Journal of Materials Chemistry A

PAPER

View Article Online
View Journal | View Issue

Cite this: J. Mater. Chem. A, 2017, 5, 19901

Trends in the phase stability and thermochemical oxygen exchange of ceria doped with potentially tetravalent metals†

Roger Jacot,[a] René Moré,[a] Ronald Michalsky,[b] Aldo Steinfeld[b] and Greta R. Patzke*[a]

Ceria is among the most prominent materials for generating clean fuels through solar thermochemical CO_2 reduction and water splitting. The main optimization parameter for ceria in solar reactors is the oxygen exchange capacity (OEC, $\Delta\delta$), which can be notably improved through various dopant types. Among them, tetravalent dopants excel through the formation of active vacancies which lead to particularly high OEC values. We thus performed a comprehensive screening evaluation of all dopants in the periodic table which have been reported to adopt an oxidation state of +IV. All thermally stable doped ceria samples, $M_{0.1}Ce_{0.9}O_{2-\delta}$ (M = Si, Ti, V, Cr, Zr, Nb, Rh, Hf, Ta, Nb, V, Pr, and Tb), were first analyzed for $\Delta\delta$ improvement with thermogravimetric analysis (TGA). Dopant solubility limits and behavior in the ceria host lattice was evaluated with scanning electron microscopy (SEM-EDX) and powder X-ray diffraction techniques. No indications for carbonate side product formation were found. Hf-, Zr-, and Ta-doped ceria display higher OEC than pristine ceria, and Raman spectroscopy indicated that their improved performance is accompanied by a higher versatility in the underlying vacancy formation processes. Furthermore, the effective dopant radii are close to an optimal dopant radius around 0.8 Å for maximum $\Delta\delta$ according to TGA cycling experiments. These experimentally derived trends for doped ceria were supported by density functional theory (DFT) calculations which analogously correlate $\Delta\delta$ with the partial electronic charge of the metal dopants.

Received 10th May 2017
Accepted 31st August 2017

DOI: 10.1039/c7ta04063f

rsc.li/materials-a

1. Introduction

Solar thermochemical splitting of CO_2 and H_2O utilizes the entire spectrum of sunlight to produce CO and H_2 (syngas) as precursors for the production of synthetic liquid hydrocarbon fuels *via* the Fischer–Tropsch process and other established gas-to-liquid technologies.[1,2] Nonstoichiometric ceria ($CeO_{2-\delta}$) has emerged as benchmark redox material for thermochemical splitting of CO_2 and H_2O through solar-driven two-step temperature/pressure-swing redox cycles (*cf.* eqn (1), (2a) and (2b)). In a first step, concentrated solar radiation is utilized in the form of high-temperature process heat to endothermically reduce ceria at high temperature and low partial pressure of O_2 (p_{O_2}) yielding oxygen vacancies in the solid phase and O_2 gas (eqn (1)). The oxygen vacancies are utilized in a second step in which ceria is exothermically oxidized to abstract oxygen from CO_2 yielding CO (eqn (2a)) or from H_2O yielding H_2 (eqn (2b)). The difference between the thermochemically stable oxygen nonstoichiometry of the redox material at oxidizing conditions (δ_{oxi}) and reducing conditions (δ_{red}) is the oxygen exchange capacity (OEC, $\Delta\delta = \delta_{red} - \delta_{oxi}$).

$$CeO_{2-\delta_{oxi}} \overset{1500\,^{\circ}C}{\rightleftharpoons} CeO_{2-\delta_{red}} + \frac{\Delta\delta}{2}O_2 \quad (1)$$

$$CeO_{2-\delta_{red}} + \Delta\delta CO_2 \overset{1000\,^{\circ}C}{\rightleftharpoons} CeO_{2-\delta_{oxi}} + \Delta\delta CO \quad (2a)$$

$$CeO_{2-\delta_{red}} + \Delta\delta H_2O \overset{1000\,^{\circ}C}{\rightleftharpoons} CeO_{2-\delta_{oxi}} + \Delta\delta H_2 \quad (2b)$$

The OEC is a key optimization parameter for rational materials design, as it correlates directly with the specific amount of fuel that can be produced per mass of solid cycled. Typically, materials design strategies aim for increasing the OEC over that of a benchmark redox material, such as $CeO_{2-\delta}$, at a specific set of process conditions. Alternatively, materials thermochemically less stable than $CeO_{2-\delta}$, such as various perovskites, are currently investigated for reaching an OEC comparable to that of $CeO_{2-\delta}$ while liberating O_2 at lower temperatures. To increase the OEC, to accelerate the redox kinetics, and to increase the

[a]University of Zurich, Department of Chemistry, Winterthurerstrasse 190, CH-8057 Zurich, Switzerland. E-mail: greta.patzke@chem.uzh.ch

[b]Department of Mechanical and Process Engineering, ETH Zurich, Sonneggstrasse 3, CH-8092 Zurich, Switzerland

† Electronic supplementary information (ESI) available: Analytical characterization of doped ceria samples (ICP-MS, Rietveld refinements, SEM-EDX mappings, UV/Vis- and FT-IR data, XAS spectroscopy). See DOI: 10.1039/c7ta04063f

thermo-mechanical stability, previous studies have considered metal cation doping of perovskites,[3–8] spinel-,[9–11] ceria,[12,13] and ceria-based[14–17] metal oxide redox materials. However, the use of different performance criteria, process conditions, and reference materials complicates a conclusive assessment of metal doping strategies.

To determine, quantify, and rationalize systematic trends in the thermo-mechanical stability and the capacity and kinetics of the oxygen exchange reactions with $CeO_{2-\delta}$, this work evaluates comprehensively all metals of the periodic system that can access the +IV oxidation state in principle, as shown in Scheme 1. We focus on tetravalent metal dopants, because they change the redox-activity of oxygen vacancies at cycle conditions without changing the oxygen nonstoichiometry at ambient conditions. Tetravalent metal dopants have been reported to improve the OEC of ceria,[18] most notably through Zr^{4+} and Hf^{4+}, which was rationalized with energy storage in the form of tensile strain of the Zr– or Hf–O bonds. When such strain is released upon oxygen vacancy formation, the endothermic character of the ceria reduction is favorably maintained.[19]

In comparison, metal dopants with oxidation states below or above +IV, especially trivalent and pentavalent ions, maintain electroneutrality through introduction of oxygen vacancies that are in principle more stable at ambient and cycle conditions. These oxygen vacancies are redox-inactive, as electrons are insufficiently promoted upon ceria reduction into the high energy Ce f-band, thereby limiting the oxidation reaction.[19] However, metal dopants that introduce stable oxygen vacancies may increase the oxygen ion conductivity[1,20,21] and redox kinetics, such as reported for 15% Sm-doped $CeO_{2-\delta}$.[22] In contrast, anti-sintering agents, such as Al_2O_3, La_2O_3, SiO_2, and Pt for (doped) ceria,[23–25] remain inert and act as "crystallite spacers" preventing $CeO_{2-\delta}$ from sintering. Since tri- and lower valent metal dopants have been well studied and are also prominent anti-sintering agents,[25,26] we newly evaluate in this work tetravalent metal dopants for their comprehensive properties.

The present screening of nominal $D_{0.1}Ce_{0.9}O_{2-\delta}$ redox materials for all potentially tetravalent metal dopants (D) is structured as follows: Section 3.1 outlines the screening strategy and limits the set of suitable dopants by experimental investigation of the thermochemical stability. Section 3.2 assesses experimentally the performance of doped ceria for solar-driven CO_2 splitting at equal cycle conditions and relative to pristine $CeO_{2-\delta}$ as a reference, employing the OEC and the rates of ceria reduction and oxidation as performance indicators. Sintering behavior and changes in the oxidation state and coordination of the dopants are discussed as well. Section 3.3 continues with screening for systematic trends and correlates the experimental data with the effective ionic radii of the dopants as given in the literature.[40] This approach is motivated by previous studies indicating a trade-off between the extent of ceria reduction and oxidation that depends on the ionic radii of the dopants.[14,26] Finally, Section 3.4 reports a linear correlation of the OEC with the partial electronic charge of the metal cation dopant at $D_{0.25}Ce_{0.75}O_2(111)$ surfaces computed *via* density functional theory (DFT). These investigations are inspired by previous DFT studies of the redox energetics for various metal oxide surfaces and bulk compositions,[35] and they are rationalized with oxide oxidation-limited redox energetics at the selected cycle conditions.

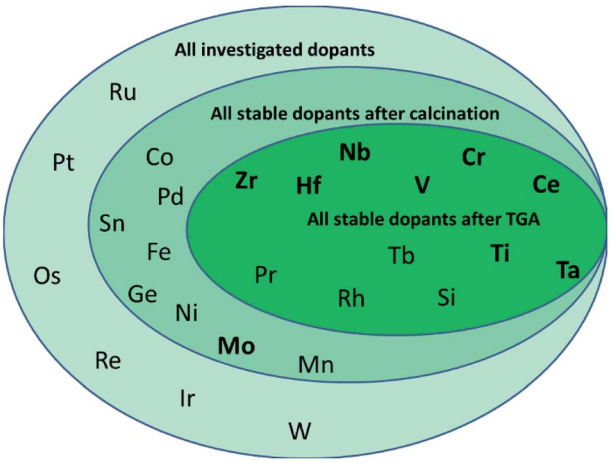

Scheme 1 Investigated metal dopants of nonstoichiometric ceria. The screening starts with all metals of the periodic system that can access the +IV oxidation state, and that are neither radioactive nor volatile at the redox cycle conditions (ceria reduction at 1500 °C in 100 mL Ar per min and ceria oxidation at 1000 °C in 50 mL CO_2 per min and 50 mL Ar per min). Dopants further investigated with electronic structure calculations are highlighted in bold.

2. Experimental section

2.1 Materials synthesis

All doped ceria samples were synthesized by a modified Pechini-type sol–gel method,[15] starting from a ratio of 1.5 mol citric acid per 1 mol metal cation. All samples were calcined at 1100 °C for 24 h. The starting materials were $Ce(NO_3)_3\cdot 6H_2O$ (99%), $ZrO(NO_3)_2\cdot 6.3H_2O$ (99%), $HfCl_4$ (99.9%), $TaCl_5$ (99.8%), $SnCl_4\cdot 5H_2O$ (98%), $MoCl_5$ (98%), WCl_4 (97%), $NbCl_5$ (99%), NH_4VO_3 (98.5%), $Cr(NO_3)_3\cdot 9H_2O$ (98%), $Pr(NO_3)_3\cdot 5H_2O$ (98%), $Tb(NO_3)_3\cdot 5H_2O$ (99.9%), $SiCl_4$ (99.0%, purchased from Merck), $Pd(NO_3)_2\cdot 2H_2O$ (~40% Pd basis, from Fluka), $H_2(PtCl_6)\cdot 6H_2O$ (~40% Pt, from Merck), $IrCl_3\cdot 3H_2O$ (99.8%, from Alfa Aesar), $RuCl_3$ hydrate (40% Ru, from Johnson Matthey & Brandenberger AG), CH_3ReCl_3 (71–76%), $OsCl_3$ (99.9%), $Co(NO_3)_2\cdot 6H_2O$ (≥98%), $Fe(NO_3)_3\cdot 6H_2O$ (99.99%), $GeCl_4$ (99.99%), $Ni(NO_3)_2\cdot 6H_2O$ (99.999%), $Mn(NO_3)_2\cdot 6H_2O$ (98% from Alfa Aesar), Rh(II)acetate (99.99%), $TiCl_4$ (99.99%), and anhydrous citric acid (99%). If not specified otherwise, chemicals were purchased from Sigma-Aldrich. If not noted otherwise, ceria doped at about 10% with a stable metal dopant (D) was evaluated further, *i.e.*, materials with an ideal $D_{0.1}Ce_{0.9}O_{2-\delta}$ stoichiometry, abbreviated for clarity with "10D".

2.2 Materials characterization

Inductive coupled plasma mass spectrometry (ICP-MS) measurements were performed with an Agilent Technologies

QQQ 8800 Triple quad ICP-MS spectrometer, equipped with a standard x-lens setting, nickel cones and a "micro-mist" quartz nebulizer (for experimental details *cf.* ESI†). The elemental compositions of the metal oxide samples were mapped by energy dispersive X-ray spectroscopy (EDX) performed on a Jeol JSM 6060 scanning electron microscope (SEM) equipped with a EDX Bruker AXS 1333 eV X Flash detector 4010 (with an acceleration voltage of 30 kV). Powder samples were dispersed in ethanol (abs.) and deposited on carbon tape which was fixed on the sample holder of the SEM. Samples were allowed to dry at ambient conditions. SEM images were then recorded on a Zeiss SUPRA 50VP SEM using the SE2 detector, an acceleration voltage of 10 kV, and a working distance of 3 mm. Powder X-ray diffraction (PXRD) patterns were recorded on a STOE STADI P diffractometer equipped with a DECTRIS MYTHEN 1K detector in transmission mode using a Ge monochromator for Cu $K_{\alpha 1}$ radiation. UV/Vis spectra of the powder samples placed into in a 0.1 mm powder cuvette were recorded on a Perkin Elmer Lambda 650S spectrometer in diffuse reflectance mode. Background calibration was performed using a standard Teflon background (labsphere certified reflectance standard USRS-99-020; AS-01159-060). FT-IR spectroscopy was performed with a Bruker Vertex 70 spectrometer equipped with a Pt ATR (attenuated total reflection) in transmittance mode. Raman spectra were recorded on a Renishaw Ramascope 1000 spectrometer equipped with a 780 nm diode laser from Renishaw with 50 mW capacity. To improve the signal to noise ratio, we used detection times of about 120 s.

2.3 Thermogravimetric cycling

Thermogravimetric analysis (TGA) of the ceria samples was conducted using a Netzsch Jupiter STA 449 F3 TGA. The measurements were performed with about 100 mg powder samples placed into a shortened Al_2O_3 crucible (Netzsch 3.4 mL GB445213). The crucible was cut 12 mm from the top, just to the beginning of the round bottom, to expose a consistently high specific sample surface area in these experiments. To consistently dry and oxidize the samples before TGA analysis (*cf.* yellow highlights in Fig. S1†), each experimental run started with oxidizing the samples in a gas flow of 45 mL O_2 per min and 190 mL Ar per min by heating at 20 °C min^{-1} to 1000 °C, hold for 10 min, and subsequential cooling at 10 °C min^{-1} to 50 °C to provide related starting conditions for each sample. All volumes are reported in this work at standard conditions, *i.e.*, 20 °C and 1 bar. This oxidation step followed 2.5 consecutive redox cycles with ceria reduction in 100 mL Ar per min at 1500 °C and ceria oxidation (*cf.* blue highlights in Fig. S1†) in a mixture of 50 mL CO_2 per min and 50 mL Ar per min (*i.e.*, $p_{CO_2} = 0.5$ bar, <0.001% O_2) at 1000 °C. We note, ceria oxidation has been shown previously to be independent on the use of excess CO_2 within a reasonable range.[27,28] The oxidation step was initiated 10 min after the sample was cooled down to 1000 °C (grey section in Fig. S1†). Ar (99.999%), O_2 (99.998%), and CO_2 (99.998%) were purchased from Garbagas.

The OEC ($\Delta\delta$) was calculated from the TGA data as the relative difference of the steady-state sample weight at reduction and re-oxidation in the second redox cycle (*i.e.* with the oxidation step 520–580 min after starting the cycling experiments, *cf.* Fig. S1† and Section 1). To represent the redox kinetics consistently for all investigated materials, we approximate the maximum rates ($r_i = |\Delta m_i|/|\Delta t_i|$) of ceria reduction ($i = r$) with the absolute mass change taken as the difference between 5% below the initial mass and 5% above the final mass ($|\Delta m_r|$) and with the equivalent materials-specific duration ($|\Delta t_r|$). For ceria oxidation ($i = o$) the absolute mass change was taken as the difference between 5% above the initial mass and 5% below the final mass ($|\Delta m_o|$) and with the equivalent materials-specific duration ($|\Delta t_o|$) as well.

2.4 X-ray absorption spectroscopy

X-ray absorption spectroscopy (XAS) and in particular X-ray absorption near edge spectroscopy (XANES) were performed at the ESRF (Swiss-Norwegian Beamline BM01B) and SLS (Super XAS beamline) on the solid samples dispersed in cellulose at room temperature. Experiments for absorption edges below 6 keV were recorded in fluorescence mode using a vortex fluorescence detector. All spectra above 6 keV were recorded in transmission mode. As standards we used CeO_2 (>99.9%), $Ce(C_2O_4)_3 \cdot 9H_2O$ (99.9%), Cr metal powder (100 mesh, 99%, Johnson Matthey & Brandenberger AG), Cr_2O_3 (>99%), CrO_2 (Magtrieve™), K_2CrO_4 (>99.5%, Merck), V_2O_3 (98%), $VO(SO_4) \cdot 5H_2O$ (99.99%), V_2O_5 (>99%), ZrN (>99%), ZrO_2 (>99%), NbO_2 (99.9%), Nb_2O_5 (99.5%), HfO_2 (>99.95%), $Pr(NO_3)_3$ (99.9%), Pr_6O_{11} (99.9% Fluka), TaC, Ta_2O_5, and $Tb(NO_3)_3 \cdot 5H_2O$ (99.9%). If not otherwise specified, chemicals were purchased from Sigma-Aldrich. Measurement calibration, and Fourier transformation of the XAS spectra were accomplished using the Athena software, while the extended X-ray absorption fine structure (EXAFS) was fitted using the Artemis software.[29]

2.5 Electronic structure computations

In order to screen for electronic and geometric contributions of metal doping at ceria surfaces to the experimentally established trend in the oxygen exchange capacity, $D_{0.25}Ce_{0.75}O_2$ (D = Ce, Ti, V, Cr, Zr, Nb, Mo, Hf, and Ta) with the cubic fluorite crystal structure were modeled *via* DFT, performed with the Grid-based projector-augmented wave (GPAW) code.[30,31]

Atomic configurations were handled in the Atomic Simulation Environment (ASE).[32,33] Exchange–correlation interactions were treated by the revised Perdew–Burke–Ernzerhof (RPBE) functional of Hammer, Hansen, and Nørskov[34] and the line search Broyden–Fletcher–Goldfarb–Shanno (BFGS) algorithm was employed to optimize the atomic geometries until the maximum force was less than 0.05 eV $Å^{-1}$. Convergence was achieved with a Fermi–Dirac smearing of 0.1 eV. Structure optimization results were extrapolated to 0 K. Modeling of metal oxides with DFT is complicated by partly localized electrons leading to correlated electronic structures. This is commonly accounted for by use of the Hubbard *U* model to modulate the electronic structure. Although we have reported previously that this modulation is not necessary to satisfactorily described the ceria surface,[35] we follow here previous computational

approaches and consistently included $U = 5$ eV for the Ce f states.[36,37]

Ceria bulk models had DCe_3O_8 stoichiometry, periodic boundary conditions in all directions, and all atoms were allowed to optimize their positions (relax). To avoid reminiscent stress in the calculations, the lattice constant of the CeO_2 bulk was chosen as the DFT-calculated lattice constant (5.543 Å), which, with a relative error <2.5%, compares well with the experimental value (5.411 Å).[38] The oxidized and reduced surfaces of the redox materials were modeled using the thermodynamically most-stable mixed-terminated $CeO_2(111)$ surface,[35] with $DCe_3O_8(111)$ and $DCe_3O_7(111)$ stoichiometry, respectively. These models contained one upper layer, that is, $DCeO_4(111)$ and $DCeO_3(111)$, respectively, that was allowed to relax and that was stacked in *z*-direction atop one lower layer $Ce_2O_4(111)$ that was constrained to the bulk geometry. The surfaces were modeled with 10 Å of vacuum perpendicular to the surface and the slabs were periodically repeated in the directions parallel to the surface. A *k*-point sampling of $4 \times 4 \times 4$ for bulk calculations and $4 \times 4 \times 1$ for surface calculations was used for sampling of the Brillouin zone.

3. Results and discussion

3.1 Screening strategy and thermochemical stability evaluation

3.1.1 Screening strategy. The screening reported here consists of three consecutive steps: in a first step we limit the set of potential metal dopants to all metals of the periodic system that can access the +IV oxidation state in solids and that are neither radioactive nor volatile at screening conditions. These boundary conditions of our screening strategy resulted in 26 potential metal dopants for ceria, which are shown in Scheme 1 along with the decrease in the eligible metal dopants after synthesis. Ce indicates un-doped $CeO_{2-\delta}$, used as a reference throughout this work.

Next, the optimized working point of a dopant concentration of 10% (Scheme 1 and Fig. S2†) was derived from our previous work[15] and from reports of maximum ionic conductivities reached at dopant concentrations in the range of 7–10%.[21] Optimization experiments (Fig. S2†) showed that the best working point for Ta-doped ceria was at slightly lower concentrations, such that the Ta content was adjusted to about 7%. Doped ceria samples were synthesized *via* the citrate-gel method[15] and calcined. The effective dopant concentrations of the ceria samples were determined by EDX after calcination for 24 h at 1100 °C in air. Ceria samples with a stable dopant concentration of about 10% were further investigated.

Finally, the effective dopant concentrations of the ceria samples were again determined by EDX after 2.5 consecutive redox cycles, with ceria reduction at 1500 °C and ceria oxidation at 1000 °C in 0.5 bar CO_2, analyzed by TGA. Ceria samples with a stable dopant concentration of about 10% were investigated further by PXRD, SEM, and various spectroscopic methods.

To determine and quantify systematic trends in the redox activity and stability of metal-doped ceria, we conclude this study by employing the experimental data to screen for systematic correlations with geometric and electronic characteristics of stable metal-doped ceria (Sections 3.3 and 3.4).

3.1.2 Metal cation stability and oxygen exchange capacity. We identified 11 stable metal-doped ceria-based materials after the first screening step, namely 10D (D = Si, Ti, V, Cr, Zr, Nb, Rh, Hf, Ta, Pr, and Tb), while the other 15 dopants evaporated either partially or fully.

The OEC of all samples was quantified by TGA, and Fig. 1 shows the temperature and mass changes recorded during the redox cycling of pure ceria, and Zr-, Hf-, and Ta-doped ceria (all other samples are shown in Fig. S1†). To assess stable integration of the metal cations into the ceria host lattice, Table 1 summarizes the chemical composition analysis using ICP-MS of the ceria samples before and after redox cycling. ICP-MS data for 10Si were omitted due to typical problems with the measurement and sample preparation of Si-containing oxides involving hydrofluoric acid treatment (Table 1).

From this data we suggest that the three most promising ceria-based redox materials are 10Zr, 10Hf, and 7Ta, since the dopant concentrations after redox cycling are constant within ±2% of the as-synthesized values and the OEC is higher than that of $CeO_{2-\delta}$ (*cf.* Section 3.4 and ESI†). The long-term stability of 10Zr, 10Hf, and 7Ta is subject to ongoing studies. The remaining eight materials, namely 10D (D = Si, Ti, V, Cr, Nb, Rh, Pr, and Tb), were stable at test conditions, except 10Si and 10Rh, as discussed below, but did not surpass the OEC of $CeO_{2-\delta}$. Therefore, these were considered in the following as references for further characterizing 10Zr, 10Hf, and 7Ta (*cf.* Section 3.2) and to investigate the general influence of the effective ionic radii on the reduction behavior and the $\Delta\delta$ of doped ceria.

10Si and 10Rh both displayed significant and irreversible mass loss during the TGA experiment and were not considered for further evaluation. EDX mapping (Fig. S9†) furthermore

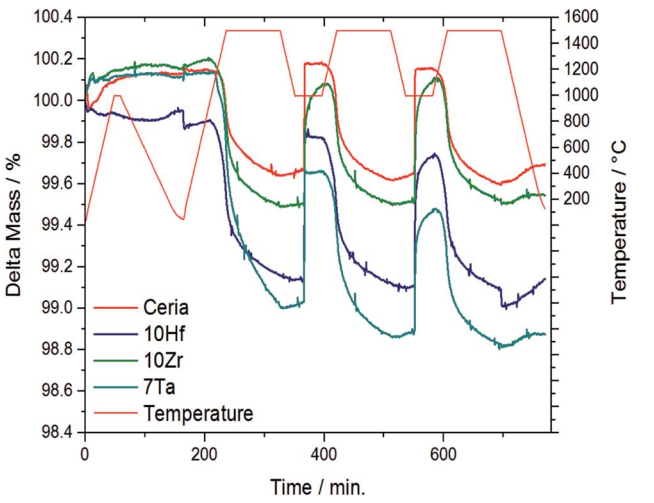

Fig. 1 Relative mass and temperature changes monitored by TGA during 2.5 consecutive redox cycles with the three most promising and stable metal-doped ceria-based redox materials, *i.e.*, 10Hf, 10Zr, and 7Ta, and $CeO_{2-\delta}$ as a reference. The complete data for all investigated materials is given with ESI.†

Table 1 Characterization of the synthesized ceria-based materials (first column) before (top value) and after (bottom value) 2.5 redox cycles as described in the text. Listed are the metal cation dopant concentration determined by ICP-MS, the lattice constant *a* determined from Rietveld refinements, and the ionic radii[40] of the given metal cation specified with its valence and coordination number. All metal cations are 8-fold coordinated if not mentioned otherwise

Sample	Dopant conc. [%] (ICP-MS)	*a*/Å	Ionic radius[40]/Å (coordination)
$CeO_{2-\delta}$	—	5.41190(4)	Ce(III) 1.143
	—	5.41108(2)	Ce(IV) 0.97
10Hf	9.8	5.38401(8)	Hf(IV) 0.83
	9.7	5.40962(4)	
10Zr	10.0	5.38428(7)	Zr(IV) 0.84
	10.1	5.41165(8)	
10Cr	9.6	5.40995(4)	Cr(III) 0.615 (6-fold)
	9.4	5.41163(6)	Cr(IV) 0.55 (6-fold)
10Nb	11.3	5.40833(9)	Nb(IV) 0.79
	12.0	5.4350(3)	Nb(V) 0.74
10V	10.4	5.41132(5)	V(IV) 0.72
	10.4	5.41229(6)	V(V) 0.54 (6-fold)
10Pr	10.2	5.4092(4)	Pr(III) 1.126
	10.3	5.43206(3)	Pr(IV) 0.96
10Tb	10.0	5.39809(4)	Tb(III) 1.04
	10.3	5.41372(3)	Tb(IV) 0.88
10Ti	10.6	5.41175(4)	Ti(IV) 0.74
	10.9	5.4138(1)	
7Ta	7.2	5.41051(6)	Ta(IV) 0.68 (6-fold)
	7.3	5.43661(9)	Ta(V) 0.74
10Rh	14.0	5.41219(6)	Rh(IV) 0.6 (6-fold)
	14.1	5.41098(7)	
10Si	—	5.41208(5)	Si(IV) 0.4 (6-fold)
		5.41179(5)	

showed the formation of metallic rhodium agglomerates. 10Tb and 10Pr also underwent a notable yet reversible mass change in the TGA experiment during the first 150 min. 10Nb, 10Cr, 10Ti, 10Zr, 10Hf, and 7Ta all displayed a higher extent of reduction than pristine ceria (*cf.* Fig. S1b†). Generally, the observed reduction kinetics are much slower than the corresponding oxidation kinetics. Only 10Zr, 10Hf, and 7Ta exhibited better re-oxidation properties than pure ceria, while the $\Delta\delta$ of 10Nb is comparable to pristine ceria. 10Zr, 10Hf, 10Nb, and 7Ta displayed slower oxidation kinetics than pristine ceria.

The extent and kinetics of the reduction are not only strongly influenced by the reduction temperature,[39] but also by the dopant type. Ta-doping, for example, seems to improve both the extent of reduction as well the kinetics. While the onset of oxidation is rather fast for all investigated materials, the effective overall kinetics depend more strongly on the individual dopants.

3.1.3 Phase purity of ceria materials. To characterize the phase purity of the synthesized redox materials and their response to the changing thermochemical environments, we recorded the PXRD spectra of the solids analyzed before and after the redox cycling (*cf.* Fig. 2). Complete Rietveld refinements of the diffraction patterns are given with ESI (*cf.* Fig. S3 and S4†). The lattice constants and ionic radii of the specific metal cations are summarized in Table 1.

Powder X-ray diffraction and Rietveld refinement showed that the following samples were phase pure and isostructural with ceria (fluorite type, S.G. $Fm\bar{3}m$) before and after TGA investigations (Fig. 1 and S3†): 10Hf, 10Zr, 10Si, 10Pr, and 10Tb. The presence of amorphous side products in 10Si, however, cannot be excluded in light of its thermal behavior during pretreatment (*cf.* Section 3.1.2). 10Ti and 10Cr are phase pure only prior to the redox cycling. After redox cycling, 10Ti and 10Cr exhibit small amounts of perovskite-related side products (*i.e.*, $CeCrO_3$ [PDF 00-075-0289] and layered $Ce_2Ti_2O_7$ [PDF 00-047-0667], respectively). A second phase prior to redox cycling was evident for 10V, 10Nb, 10Rh, and 7Ta. As-synthesized 10V contained $CeVO_4$ (PDF 00-012-0757; S.G. $I4_1/amd$). 10Nb contained Ce_3NbO_7 (PDF 00-023-0144) before redox cycling, which had turned into scheelite-type $CeNbO_4$ (PDF 00-033-0332) after redox cycling. Furthermore, 10Rh contained Rh (PDF 00-005-0685), in agreement with the EDX mapping (*cf.* Fig. S9†), and $CeTa_3O_9$ (PDF 00-045-1212; S.G. *Pnma*) was present in 7Ta.

3.1.4 Metal cation solubility in ceria. To assess the effect of the variable thermochemical conditions of the CO_2 redox splitting cycles on the homogeneity and morphology of the metal cation-doped ceria powders, we employed EDX to record the spatial elemental distribution in the solid phase before and after the TGA-tracked redox cycling. The complete elemental mapping is shown with Fig. S9.†

Evenly colored EDX mappings indicate a fairly homogeneous elemental distribution for the 10Hf, 10Zr, 10Pr, and 10Tb samples, which is in line with the PXRD results. This is contrasted to some degree by the less homogeneous characteristics of the remaining ceria samples. Occurrence of a second crystal phase after the TGA treatment in 10Cr and 10Ti (*cf.* above) is clearly confirmed by the respective elemental mappings (Fig. S9†). In contrast to the PXRD pattern shown in Fig. 2, the as-synthesized 10V appears fairly homogeneous, while the post-TGA sample displays large regions with increased vanadium concentrations. As-synthesized 10Nb already displays a rather low homogeneity of the elemental distribution. This is quite different to 10Ti, which displays notably decreased homogeneity only after the redox cycling. However, taking into account the moderate sampling depth of EDX and considering the agglomerate-like appearance of the inhomogeneous areas in 10Ti after redox cycling, it cannot be excluded that these inhomogeneous areas are only surface features. Similarly, the second crystal phase is not very pronounced in 7Ta after the redox cycling (see weak additional peaks in Fig. 2b). 10Si shows distinct areas with increased oxygen concentrations, which could be rationalized with the presence of an amorphous silicon oxide phase that does not appear in the PXRD pattern (*cf.* Fig. 2). In line with the PXRD measurements, the EDX analysis suggests formation of spherical metallic particles in 10Rh that are clearly visible in the element mappings before and after TGA, going hand in hand with less pronounced grain growth. This rather unique case of dopant agglomeration as a metallic phase has the potential for further applications as an anti-sintering agent to replace the more expensive platinum.[23,41,42] Additionally, the present synthetic route may offer a stable ceria matrix for high-temperature applications of metallic rhodium catalysts.[43,44]

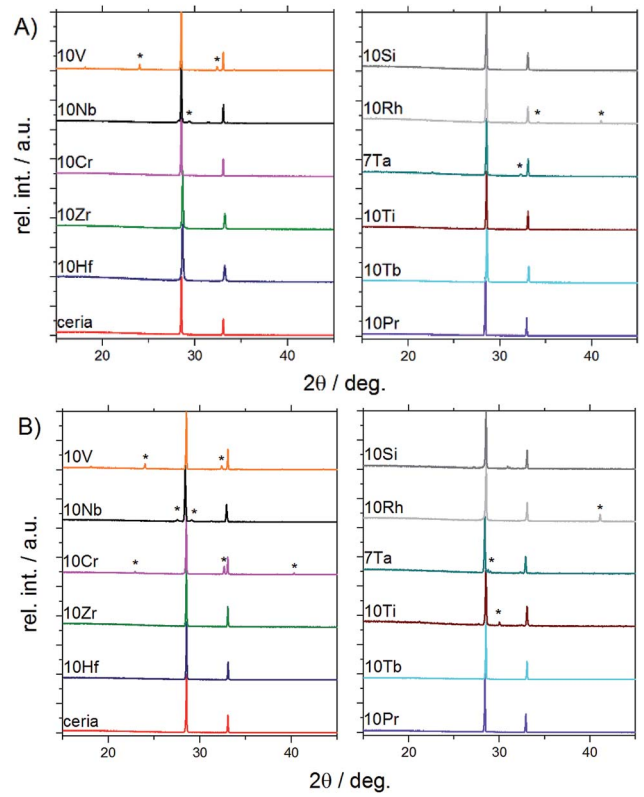

Fig. 2 PXRD patterns of doped ceria-based materials before (A) and after (B) redox cycling tracked by TGA (for Rietveld refinements and magnifications into the range from 28° to 29° *cf.* Fig. S3 and S4†).

In summary, PXRD and EDX mapping results demonstrate that among the 26 investigated possible dopants only Zr, Hf, Pr, and Tb form phase-pure, homogeneous, and thermally stable ceria-based materials with stable contents of approx. 10% metal cation dopant. 10Si and 7Ta display a low to moderate extent of dopant agglomeration and side product formation, while this effect is more pronounced in 10Cr, 10Rh, 10Ti, 10Nb, and 10V.

3.2. Characterization of ceria before and after CO_2 reduction

3.2.1 Agglomeration and sintering (SEM). Selected SEM images monitoring the sintering behavior of doped ceria before and after TGA are compared to undoped ceria in Fig. 3 and S6.† Pristine ceria shows only minor sintering effects before and after TGA.

7Ta and 10Rh do not undergo much sintering either, the latter being probably stabilized by metallic Rh particles as discussed above. 10Hf (Fig. 3d), 10Pr (Fig. S6p†), 10Tb (Fig. S6r†), and 10Si (Fig. S6v†) undergo notable sintering only after TGA treatment. Weak sintering compared to pristine ceria after synthesis followed by stronger sintering and grain growth upon TGA investigations was observed for 10Zr (Fig. 3e and f) and 10 Cr (Fig. S6i and j†). The remaining samples were already significantly sintered before TGA and displayed further grain growth and agglomeration, as can be seen for 10Nb (Fig. S6k and l†), 10V (Fig. S6m and n†), and 10Ti (Fig. S6s and t†).

3.2.2 Band gap energies and surface composition (UV/Vis and FT-IR). Direct band gap energies were determined with UV/Vis spectroscopy (Fig. S7†) for the strongest absorption band around 350 nm, and they are in the 3.1–3.3 eV range for all samples. These values decrease slightly to *ca.* 2.9–3.2 eV after TGA (Fig. S7;† except for 10Nb, 10V, 10Tb, 10Pr, 10Ti, and 7Ta where absorption was too pronounced for reasonable data evaluation). All band gaps are in reasonable agreement with the literature value of 3.1 eV reported for pure ceria.[45] The Ce^{4+} to Ce^{3+} charge transfer band at 588 nm (ref. 45) appears to be present only in 10Cr so that it is most likely rather arising from chromium centers. Given that only little further information about the electronic structure of doped ceria samples can be extracted from the present UV/Vis spectra due to the overlapping bands and the strong absorption (for details see ESI†), the valence states of dopants and ceria matrix were derived from XANES data (see below).

All samples were analyzed with FT-IR spectroscopy for possible residual carboxylate/carbonate species from the citric acid precursor (Fig. S8†) as well as for CO_2 adsorption as a frequently encountered side reaction of perovskite materials during solar thermochemical applications.[46] No significant indications for carbonate formation were found, and a detailed discussion of the FT-IR spectra can be found in the ESI.†

Metal–oxygen bonds and lattice defects in ceria have been characterized in detail by Raman spectroscopy.[47–50] In contrast to the 524.5 nm laser used in previous studies,[15] spectra were recorded with a 780 nm diode laser to obtain more detailed subsurface information due to enhanced penetration depth. Raman spectra of all phase pure samples are compared to pristine ceria in Fig. 4. Pristine ceria with idealized cubic geometry displays only a single Raman peak at 464 cm^{-1} arising from the triply degenerate F_{2g} mode of the fluorite structure.[47,47] The shape of the F_{2g} mode depends strongly on the particle size and undergoes broadening together with a shift toward lower wavenumbers with increasing particle size.[48,48] This breathing mode of the oxygen atoms around cerium can become asymmetric and give rise to a shoulder around 570 cm^{-1} through replacement of Ce^{4+} cations by dopants or vacancies, which can decrease in intensity again with growing crystallite size.[50]

This shoulder is also described in ref. 47 for Pr-doped ceria, while at the same position for Sm-doped ceria two weaker bands at 546 and 600 cm^{-1} are described, which arise from another type of stable oxygen vacancies to compensate the charge difference.[47] These two bands are also observed in 10Tb after TGA treatment, but not for 10Pr after TGA. Instead, 10Pr after TGA displays a band at 570 cm^{-1} which points to the replacement of Ce(IV) with dopants and/or oxygen vacancies.[47] The generally stronger tendency of praseodymium towards the formation of tetravalent ions might favor the formation of oxygen vacancies which remain in thermodynamic equilibrium with the ceria lattice, while trivalent terbium ions give rise to more stable oxygen vacancies within the ceria matrix. A further band at 305 cm^{-1} can only be observed in 10Hf, 10Zr, and 7Ta after TGA treatment due to overlap with the broadened F_{2g} mode. This band arises from oxygen atoms which are displaced

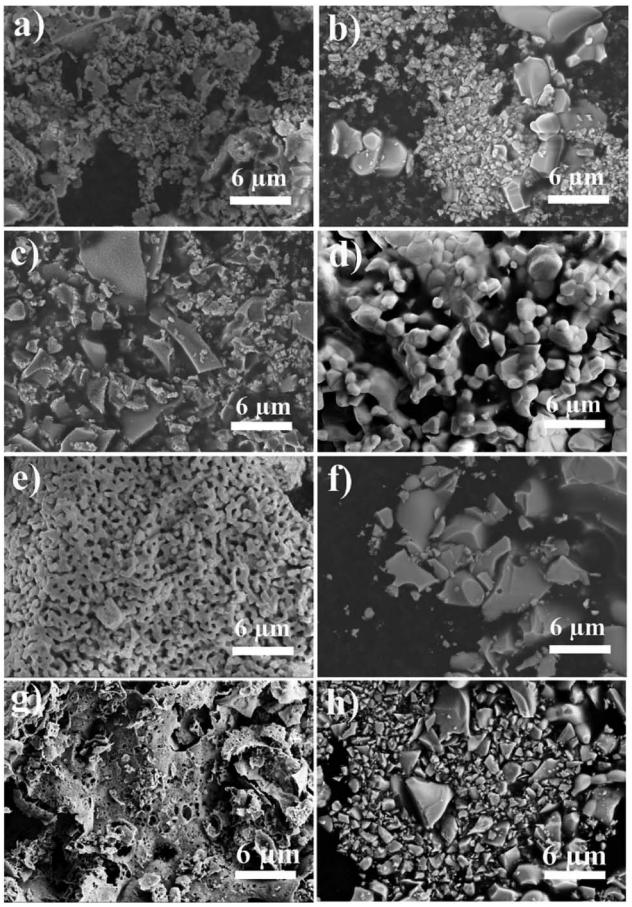

Fig. 3 Representative SEM images of selected samples before (left) and after TGA (right) of pristine ceria (a, b), 10Hf (c, d), 10Zr (e, f), and 7Ta (g, h).

from their ideal position in the ceria lattice. All three samples (10Hf, 10Zr, and 7Ta) with the highest OEC show also the most distinguished bands at 305 cm^{-1}.[48]

3.2.3 Dopant oxidation state and coordination (XANES and EXAFS). The oxidation state of 10Cr, 10Nb, 10V, 10Pr, 7Ta, and 10Tb was investigated with (XANES) before and after TGA experiments. 10Hf and 10Zr were included as tetravalent references showing no change in the dopant valence after thermal treatment (Fig. 5, Table 2), in line with their continuous thermal behavior (Fig. 1). 10Pr and 10Tb exhibit a doublet peak structure in the pre-TGA XANES spectra (Fig. 5) which indicates the presence of Ln(IV) cations.[51] The disappearance of these doublet peaks after TGA indicates a complete reduction to Pr(III) and Tb(III), respectively. We here refer to literature data due to a lack of stable Ln(IV) standards for the XANES experiments. This behavior is in line with the observed mass loss between 19 and 130 min at 400 °C during the initial TGA treatment as well as with the behavior around 200 min during the subsequent TGA cycle (Fig. S1†). The K-edge XANES spectrum of 10Cr is shown in Fig. 6, and the entire spectrum after TGA indicates significant changes in the local coordination of the chromium ions. Unfortunately, the close proximity of the chromium K-edge and the cerium L_3-edge prevents a detailed EXAFS analysis. The edge position shifts to higher energies (Fig. 6) together with comparison to selected references indicates the presence of Cr(III) before TGA and its conversion to Cr(IV) after TGA. This result is interesting, because Cr(III) would be the expected stable oxidation state, and it is moreover in line with previous XPS measurements.[52]

XANES K-edge data of 10V show a significant pre-edge peak at 5468 eV (Fig. S10†) which arises from the symmetry forbidden 3d ← 1s transition,[53] *i.e.* the vanadium ions do not display a centrosymmetric coordination. Comparison to references indicates the presence of stable vanadium(V) centers before and after TGA. However, the non-centrosymmetric coordination in combination with PXRD patterns (Fig. 2) and EDX mappings (Fig. S9†) indicates that the vanadium dopant ions are not incorporated into the ceria lattice to a large extent.

The niobium K- and tantalum L_3-edge XANES spectra of 10Nb and 7Ta do not display a significant shift of the edge position before and after TGA (Fig. S11† and 7). Comparison of the first derivative of these spectra with tetra- and pentavalent references compounds indicates that niobium and tantalum remain pentavalent throughout. This is in line with the absence of unexpected mass changes during TGA (Fig. 1).

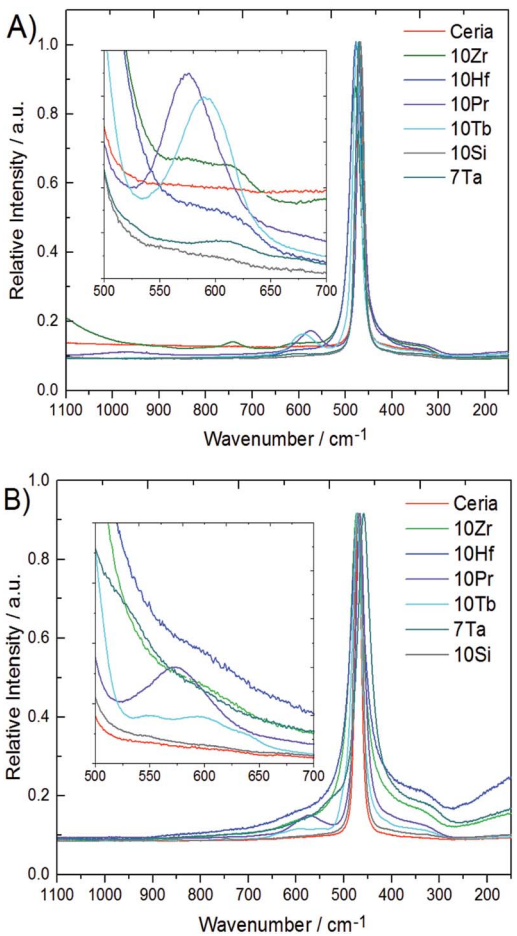

Fig. 4 Raman spectra before (A) and after (B) TGA cycling of selected doped ceria samples.

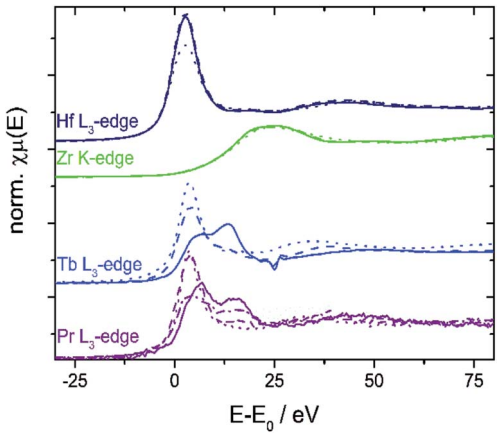

Fig. 5 XANES spectra of doped ceria samples (solid line: before TGA; dashed line: after TGA; dotted line: selected reference spectra of HfO_2, ZrO_2, $Tb(NO_3)_3$, and Pr_5O_{11}). XANES spectra of 10Tb and 10Pr show reduction of the dopant during TGA (*cf.* text).

Further structural investigations were conducted for 10Zr and compared with 10Nb. The EXAFS region of 10Zr was fitted against a structural model generated from room temperature crystallographic data for $CeO_{2-\delta}$ through substituting a single Ce atom in the elemental cell by zirconium. Lattice parameters and interatomic distances for this model were obtained from Rietveld refinement of experimental PXRD data. Reasonable fitting results with a *R* value of 2.8% were obtained (Fig. 8).

Table 2 X-ray $L_{3/2}$ absorption parameters for 10Hf and HfO_2 as well as K-edge absorption for 10Zr *vs.* standards

Sample	E_a/eV	White line/eV	Edge width/eV	Valence
Hf L_3 edge				
10Hf before TGA	9558.85	9562.19	3.34	4
10Hf after TGA	9558.85	9562.17	3.32	4
Reference Hf(IV)O_2	9558.68	9562.21	3.53	4
Hf L2 edge				
10Hf before TGA	10 736.69	10 739.32	2.63	4
10Hf after TGA	10 736.63	10 739.31	2.68	4
Hf(IV)O_2	10 736.60	10 739.18	2.58	4
Zr K edge				
10Zr before TGA	18 013.80	180.23.79	9.99	4
10Zr after TGA	18 014.13	18 024.07	9.93	4
Zr(IV)O_2	18 014.32	18 022.05	7.72	4
Zr(III)N	18 005.43	18 017.79	12.36	3
Cr K edge				
10Cr before TGA	5999.5	6007.1	7.6	3
10Cr after TGA	6003.1	6005.2	2.1	4
Cr(III)$_2O_3$	5999.2	6010.2	11	3
Cr(IV)O_2	6002.8	6009.5	6.7	4
Ta L3 edge				
7Ta before TGA	9885.0	9889.5	4.5	5
7Ta after TGA	9884.4	9887.2	2.8	5
Ta(IV)C	9882.9	9886.5	3.6	4
Ta(V)$_2O_5$	9884.7	9888.3	3.6	5

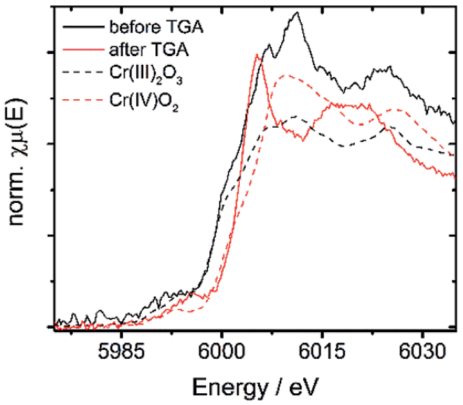

Fig. 6 XANES spectra of 10Cr before and after TGA *vs.* Cr(III) and Cr(IV) containing references.

A comparison of the EXAFS region plotted in *k*-space for 10Zr and 10Nb clearly shows differences in the local coordination of zirconium and niobium, especially the absence of a peak at 3.5 Å in the Fourier transform magnitude of 10Nb (Fig. 9).

The valence state of cerium in selected samples before and after TGA was determined from L_3-edge XANES spectra applying a linear combination fit (LCF) with reference spectra of cerium(III) oxalate, $Ce(C_2O_4)_3$, and cerium(IV) sulfate, $Ce(SO_4)_2$. The normalized absorption and the first derivatives were reconstructed with these LCFs (see Fig. 10 as a representative example). The results are summarized in Fig. 11.

Comparison of the XANES-derived ceria valences with the corresponding lattice constants derived from Rietveld refinement data for before TGA and after about three cycles (Fig. S3† and Table 1) sheds more light on the influence of ionic radii on the thermochemical performance. In the first place, decreasing oxidation states of the ceria ions are expected to result in larger lattice constants on the basis of simple ionic radii differences between Ce(III) and Ce(IV) (*cf.* values in Table 1).

This is the case for 10Zr where no dopant valence changes occur after TGA. Likewise, 10Hf shows first a decrease in lattice constants due to the incorporation of the smaller Hf(IV) cation (Fig. 10), but a larger lattice constant after TGA, probably due to the higher Ce(III) content. 10Nb also remains pentavalent, so that the observed increased lattice constants are likely due to the higher Ce(III) contents after TGA.

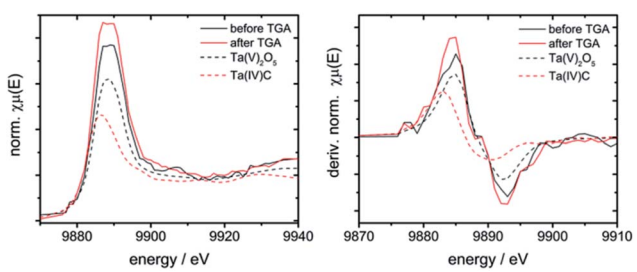

Fig. 7 Left: XANES spectra of 7Ta before and after TGA *vs.* Ta(IV) and Ta(V) containing references; right: first derivative of these spectra.

Under the assumption that a certain amount of chromium ions might still be incorporated into the ceria lattice, the absence of a significant lattice constant change in pre-/post-TGA 10Cr could be explained through opposite radii trends for ceria and chromium ions, which are canceling each other out, namely the contraction upon oxidation of Cr(III) to Cr(IV) *vs.* the formation of larger Ce(III) from Ce(IV). The same applies for 10Pr and 10Tb, where a tendency towards higher Ce(IV) contents after TGA goes hand in hand with the formation of larger Ln(III) ions. The influence of this redox process on the ceria performance is discussed in more detail below. However, other factors beyond mere ionic radii may also influence the observed lattice constant trends.

3.3. Ceria performance and stability *versus* dopant cationic radii

3.3.1 Dopant solubility and phase purity of ceria materials. The effective ionic radius of the dopants crucially influences their solubility in the ceria matrix. Generally, the solubility tends to decrease for smaller effective ionic radii,[26] giving rise to the formation of frequently perovskite-related side products. The significant amounts of a second phase in 10Cr after TGA illustrate this trend quite clearly, because the initial oxidation state of Cr(III) (0.615 Å) increases to Cr(IV) (0.55 Å) after TGA as evident from XANES analyses (*cf.* above). This goes hand in hand with the occurrence of a second phase in the PXRD pattern (Fig. 2b).

10Nb, 10Rh, and 7Ta display smaller amounts of a second phase before and after TGA in the PXRD patterns (Fig. 2), while 10V displays higher contents of a side product. XANES measurements show that Nb(v) and V(v) retain their oxidation states and effective radii of 0.74 Å and 0.54 Å, respectively. This suggests that ionic radii above 0.74 Å are favorable for the formation of phase pure solid solutions with ceria, while the preference for 4- or 6-fold coordinations among the smaller dopants favors the formation of more stable side products.[26]

10Pr and 10Tb show complete solubility of the dopants in the ceria lattice even though their oxidation states change after TGA from +IV to +III, going hand in hand with an increase of their effective ionic radii from 0.96 Å (Pr^{4+}) and 0.88 Å (Tb^{4+}) to 0.99 Å (Pr^{3+}) and 1.04 Å (Tb^{3+}), respectively. The smaller effective radii of the dopants in phase pure 10Hf and 10Zr (0.83 Å for Hf^{4+} and 0.84 Å for Zr^{4+}) narrow down the suitable radius range for dopant solubility to 0.74–0.84 Å. These results are well in line with calculated solubility trends.[26]

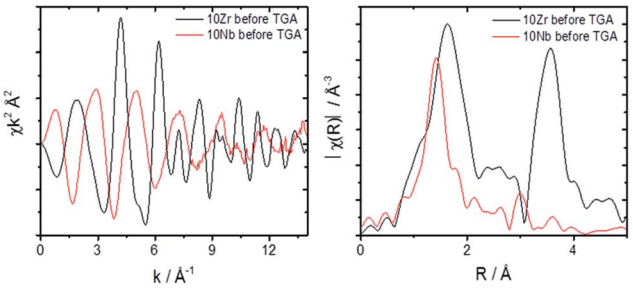

Fig. 9 EXAFS comparison of 10Zr and 10Nb in *k* space and for Fourier transformed data.

3.3.2 Sintering and redox kinetics. Comparison of the SEM measurements (Fig. 3) with the TGA results (Fig. 1) does not show a direct correlation of the sintering extent with the performance of the redox material in either the reduction step or the oxidation step. Generally, slower kinetics in the TGA cycling experiment result in flatter slopes of the TGA mass difference curve (*cf.* second oxidation steps of 10Zr, 10Zr, and 10Hf after 560 min in Fig. 1). However, the slower oxidation kinetics of 7Ta deviate from this trend (*cf.* SEM image in Fig. 3) and some materials clearly sinter while their oxidation kinetics do not decrease (*cf.* Fig. 3 and 1).

Some previous studies on doped ceria indicate that sintering, as tracked by SEM images, is not always correlated with changes in the according BET values.[15] Here, crystallite sizes derived from the Scherrer equation before and after TGA (Fig. S5†), were neither clearly correlated with the sintering effects evident from SEM images nor with the TGA oxidation kinetics. This suggests that the redox steps occur to a large extent in the ceria bulk. Preceding works indeed indicated that the amount of Ce^{3+} is rather stable and constant at temperatures above 700 °C with little influence of p_{O_2} and temperature.[54] While the majority of Ce^{3+} cations are located at the surface at temperatures below 700 °C, their concentration in bulk and surface is almost equal around 1000 °C. Therefore, charge transfer processes were reported as the rate limiting step for the redox reactions.[39]

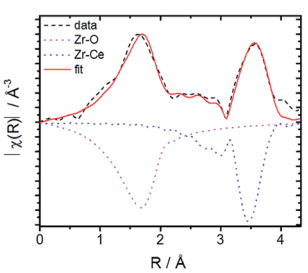

$r_{Zr\text{-}O}$ / Å	2.22 ± 0.01
$\sigma^2_{Zr\text{-}O}$ / Å^{-2}	(11 ± 2) · 10^{-3}
$r_{Zr\text{-}Ce}$ / Å	3.796 ± 0.007
$\sigma^2_{Zr\text{-}Ce}$ / Å^{-2}	(7.7 ± 0.7) · 10^{-3}
r-factor	2.8 %

Fig. 8 Fourier transform magnitudes of the EXAFS region for 10Zr and for the EXAFS fit (*cf.* text). The negative signals represent the major scattering paths (right). Experimental results were taken from EXAFS data for 10Zr before TGA (left).

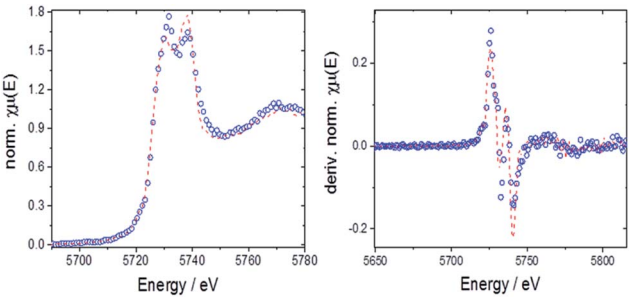

Fig. 10 Left: LCF for 10Hf before TGA with normalized absorption (open circles: experimental data, dashed line: fit); right: LCF for derivative of the normalized absorption.

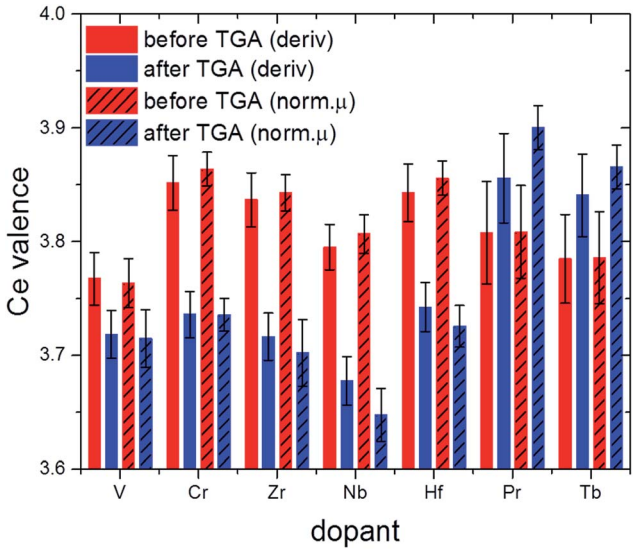

Fig. 11 Effective valence of Ce in selected samples after calcination (red) and after 2.5 TGA cycles (blue; *cf.* also Fig. 1).

3.3.3 Oxygen exchange capacity. All in all, hafnium and zirconium are the only dopants among the present screening study which remain both tetravalent and phase pure before and after TGA cycling tests. 10Nb and 10V do not only display the presence of a second phase but also significant deviations of the XANES/EXAFS spectra from their expected dopant environments in the ceria lattice. Therefore, they were not further considered in the following. Fig. 12 shows correlations between the effective ionic radii and the oxidation/reduction extents after the first and second TGA cycle, respectively.

The deviation of 10Pr and 10Tb from the remaining doped ceria samples in the depiction of the initial reduction cycle (Fig. 12a) is clearly due to their reduction from Ln(IV) to Ln(III) (*cf.* TGA cycles displayed in Fig. S1†). The significant mass loss during the initial 50 min is most likely due to this lanthanide reduction step, while the subsequent mass increase during the pre-treatment step (50 to 150 min) indicates a re-oxidation from Ln(III) to Ln(IV) through the applied carrier gas mixture for the follow-up step (Ar with 20% O_2). The subsequent reduction step of the first TGA cycle was carried out in pure Ar, initiating another mass loss accompanying the reduction of Ln(IV) to Ln(III) around 900 °C, as observed during the pre-treatment. Given that these dopant redox processes interfere with the first TGA cycle, 10Pr and 10Tb are not to be considered for the trends derived from Fig. 12a. The extent of reduction during the first TGA cycle for the other samples increases with decreasing ionic radius of the respective dopant. Up to date, this correlation has only been put forward in few studies: one of these works was mainly based on TGA cycling experiments and another study on DFT calculations.[14,26]

A straightforward electrostatic explanation for the productive effect of smaller dopants can be given in terms of reduced lattice strains. The increasing amounts of larger Ce^{3+} ions formed during the reduction step exert strain forces, which can be compensated through the presence of dopants with smaller ionic radii, thereby facilitating further oxygen release (eqn (1)).[18] However, if the effective dopant radius is below a certain value, reoxidation can be hindered, *i.e.* the equilibrium is shifted towards the reduced products. This is evident from the second TGA cycle of 10Cr (Fig. 12b and c), which exceeds 10Hf and 10Zr with respect to reduction during the first cycle but does not undergo complete reoxidation after the first two cycles. The plot of reduction extents *vs.* effective dopant radii during the second TGA cycle provides further guidelines for the optimum dopant radius which facilities the reduction with respect to pure ceria without inhibiting the re-oxidation.[55] Fig. 12b indicates that this ideal effective dopant radius is around 0.8 Å, *i.e.* close to Hf^{4+} in 8-fold coordination.

Kinetic trends for reduction and oxidation of doped ceria materials as a function of the effective dopant radii are displayed in Fig. 12c and d. Here, both processes rather tend towards a linear dependence on the dopants than to a volcano-like plot as observed for the extent of reduction (Fig. 12b).

3.4. Oxygen exchange capacity *versus* charge distribution

The OEC of a redox material is one of the most central quantities determining the performance of a solar thermochemical fuel synthesis process. Favorably high values correlate directly with relatively high fuel concentrations and relatively low heat losses from heating and cooling of solids, and, in turn, relatively high solar-to-fuel energy conversion efficiencies and thereby lower capital investment costs for solar concentrators required to produce a specific amount of solar fuel per day. To understand the origin of the trends in the OEC of doped ceria redox materials, this section employs DFT to model the mixed-terminated (111) facet of $D_{0.25}Ce_{0.75}O_{2-\delta}$ (D = Ce, Ti, V, Cr, Zr, Nb, Mo, Hf, and Ta), with $\delta = 0$ for oxidized surfaces and $\delta = 0.25$ for reduced surfaces. We note, this approach does not account for the variable solubility limits of metal cations in the bulk or at the surface, crystal phase changes in the presence of the dopant, or the dependence of the surface phase diagram on

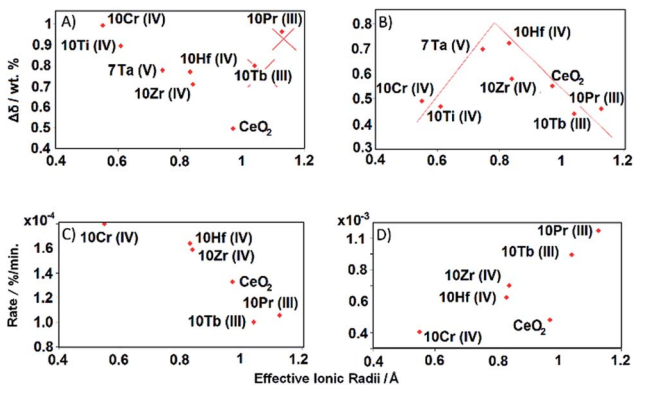

Fig. 12 Reduction extent, kinetics, and OEC of doped ceria *vs.* effective (valence dependent) ionic dopant radii: (A) reduction extent during the first cycle after full oxidation (from 150 to 230 min), (B) OEC between two full redox cycles (from 320 to 360 min), (C) reduction rate at 1500 °C, and (D) oxidation rate during the second cycle (from 320 to 360 min).

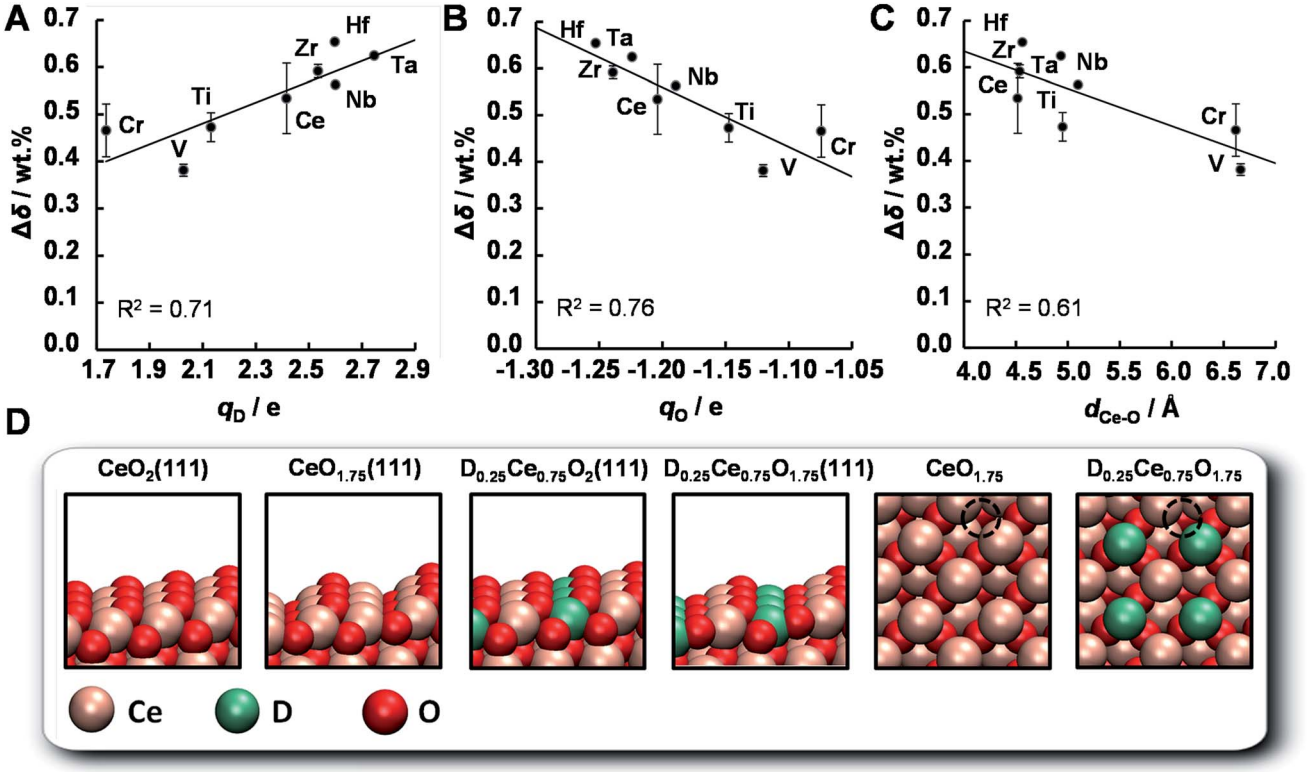

Fig. 13 Correlations of the experimentally determined OEC for $D_{0.1}Ce_{0.9}O_{2-\delta}$ (with ceria reduction at 1500 °C, and ceria oxidation at 1000 °C and 0.5 bar CO_2 in Ar), $\Delta\delta$, with the theoretically calculated partial electronic charge of (A) the metal cation dopant at the, q_D, (B) the oxygen anion, q_O, and (C) the shortest bonding length between the Ce cations and the O anions that form oxygen vacancies, d_{Ce-O}, all determined for the oxidized $D_{0.25}Ce_{0.75}O_2(111)$ surface (D = Ce, Ti, V, Cr, Zr, Nb, Hf, and Ta, as marked on the plots). Error bars indicate the experimental error calculated as one standard deviation. (D) A schematic representation of all employed DFT models with dashed lines marking the position of oxygen vacancies in the bulk.

p_{O_2}, p_{CO_2}, the total pressure, and temperature.[36,56] Since this is beyond the scope of this work, we refrain from estimating thermochemical and kinetic quantities, such as reaction enthalpies and reaction rates. As we expect the first layer of the surface to exhibit the most significant changes in the electronic structure due to metal doping and coordination, this approach is solely employed to compute relative changes in the atomic coordination, and the partial charge density was determined for all metal oxide models *via* Bader decomposition.[57] This utility of the ceria surface models is supported by the agreement between the computed and experimentally established trends, discussed in the following.

The OEC quantifies the trade-off of energy required for breaking bonds between metal cations and lattice oxygen to form O_2 and energy liberated when forming these bonds to reduce CO_2 into CO. Fig. 13 shows the experimentally measured OEC, $\Delta\delta$, *versus* the theoretically calculated partial electronic charge (in units of the elementary charge, e) of (A) the metal cation dopant at the oxidized surface, q_D, (B) the oxygen anion at the oxidized surface, q_O, and (C) the shortest bonding length between the Ce cations and the O anions that form oxygen vacancies at the oxidized surface, d_{Ce-O}. Fig. 13d shows the employed DFT models schematically. We note, $\Delta\delta$ was calculated as the difference between the maximum and minimum mass of the materials with $D_{0.1}Ce_{0.9}O_{2-\delta}$ composition, reduced at 1500 °C in 1 bar Ar and oxidized at 1000 °C in 0.5 bar CO_2 in Ar. Furthermore, d_{Ce-O} was calculated as $d_{Ce-O} = (dx^2 + dy^2 + dz^2)^{1/2}$, with dx, dy, and dz being the specific spatial contributions of the distance between the nuclei of the Ce cations and the O anions that form oxygen vacancies at the $D_{0.25}Ce_{0.75}O_2(111)$ surfaces.

We find that the OEC of ceria doped with Zr, Nb, Hf, and Ta is higher than that of the pure $CeO_{2-\delta}$ reference. This is in line with the above experimental results. While this beneficial effect of doping with Zr and Hf on the OEC of ceria is furthermore in agreement with previous reports,[15] the benefit when doping with Nb and Ta deserves further studies. As a general trend, the OEC increases with increasing net-positive charge accumulated at the metal dopant (Fig. 13a) and increasing net-negative charge accumulated at the oxygen anions (Fig. 13b). We find that larger charge separation leads to a larger OEC. This trend can be understood from the dependence of the enthalpy change of reduction on the oxygen nonstoichiometry,[58] suggesting oxide oxidation-limited thermochemistry at these conditions. For undoped ceria oxidized at 1000 °C in 0.5 bar CO_2 and reduced at 1500 °C in 1 bar Ar we find $\Delta\delta = 0.53$ wt%, *i.e.*, $\Delta\delta = 0.028$. This is in accord with typically implemented $\Delta\delta = 0.03$,[59,60] and correlates with a partial molar enthalpy change of

reduction of about 450 kJ mol^{-1}.[58] Utilizing the previously established design principle of balanced redox energetics,[35,61] we find nonstoichiometric ceria exhibits a nearly ideal energetic trade-off. This can be seen from the limiting free energy change of the redox cycle, which is due to the oxide oxidation, approaching the minimum value at these high-temperature conditions. This, in turn, suggests minor changes in the enthalpy change of reduction may determine whether the fuel synthesis thermodynamics are limited by endothermic O_2 evolution or exothermic fuel production. In principle, the enthalpy change of reduction of nonstoichiometric ceria can be controlled by process parameters, such as 425–475 kJ mol^{-1} *via* the reduction temperature and/or p_{O_2} to establish $\Delta\delta$ in the range of 0.014 to 0.056, or materials properties, such as 380–400 kJ mol^{-1} *via* metal doping to establish $\Delta\delta = 0.03$ with $CeO_{2-\delta}$ doped with 5 mol% Zr^{4+}.[58] Screening, on the other hand, for trends in the OEC with geometric factors of the electronic structure of these metal oxides, we find a weak correlation with the shortest bonding length between the Ce cations and the O anions that form oxygen vacancies at the oxidized surface (Fig. 13c). An apparent trend of the OEC decreasing with increasing d_{Ce-O} is suggested only due to the slightly lower OEC for Cr- and V-doped materials, relative to the OEC of all other investigated materials. Thus, we conclude, the extent of the net-oxygen exchange that can be established at thermodynamic equilibrium with the investigated $CeO_{2-\delta}$ materials doped with metal cations is dominated by the amount of electronic charge that is donated by the metal cations to the oxygen anions, provided that the cations remain stably incorporated under operational conditions.

4. Conclusions

Comprehensive screening of 26 eligible dopants capable of forming tetravalent cations revealed clear empirical trends for optimizing the oxygen exchange capacity, $\Delta\delta$, of ceria. Of all investigated dopants, only Hf, Zr, Pr, and Tb formed thermally stable and homogeneous doped ceria materials with approx. 10% dopant content. Ceria samples doped with Hf, Zr, Ta, and Nb all displayed comparable or higher $\Delta\delta$ values than pristine ceria during TGA screening. Further cycling experiments and PXRD investigations identified Hf, Zr, and Ta as the most promising candidates for the optimization of commercial ceria materials in solar reactors. The majority of doped ceria materials synthesized in the present study were checked for carbonate formation with various spectroscopic techniques, and no side products were found. Raman spectroscopy investigations showed that the higher performance of Hf-, Zr- and Ta-doped ceria went hand in hand with more versatility in the underlying oxygen vacancy formation processes. X-ray absorption spectroscopy was performed on Hf-, Zr-, Ta-, Nb-, Cr-, V-, Pr-, and Tb-doped ceria before and after CO_2 reduction to determine the effective dopant valences. The emerging correlation between the effective dopant radii and the observed OEC provides a sound empirical foundation for the selection of efficient ceria dopants based on straightforward electrostatic criteria. The present data set points to an optimal dopant radius around 0.8 Å for maximum $\Delta\delta$. Given that none of the available dopants precisely matches with this ideal value, combinations of two dopants with an average radius of 0.8 Å are now being screened. As the averaged conductivity of doped ceria can be improved with related strategies beyond average properties without significant co-doping effects,[62] this perspective is likely to succeed. Furthermore, the empirical doping trends were corroborated with DFT calculations pointing into the same direction. In summary, the present combined approach provides clear guidelines for the optimization of ceria materials suitable for the solar redox thermochemical cycle.

Conflicts of interest

There are no conflicts to declare.

Acknowledgements

This work was supported financially by the Swiss National Science Foundation (Grant No. 200021_162435), the University Research Priority Program (URPP) for Solar Light to Chemical Energy Conversion (LightChEC), and the European Research Council under the European Union's ERC Advanced Grant (SUNFUELS, No. 320541). Electronic structure calculations were conducted at the High-Performance Computation cluster of ETH Zurich. We thank Hermann Emerich (ESRF Grenoble), Dr Nicolo Azzaroli, and Dr Grigory Smolentsev (SLS, Villigen) for beamline support.

References

1 J. R. Scheffe and A. Steinfeld, *Mater. Today*, 2014, **17**, 341–348.
2 M. Romero and A. Steinfeld, *Energy Environ. Sci.*, 2012, **5**, 9234–9245.
3 A. H. McDaniel, E. C. Miller, D. Ari, A. Ambrosini, E. N. Coker, R. O'Hayre, W. C. Chueh and T. Jianhua, *Energy Environ. Sci.*, 2013, **6**, 2424–2428.
4 A. Demont, S. Abanades and E. Beche, *J. Phys. Chem. C*, 2015, **118**, 12682–12692.
5 S. Dey, B. S. Naidu, A. Govindaraj and C. N. R. Rao, *Phys. Chem. Chem. Phys.*, 2015, **17**, 122–125.
6 A. H. McDaniel, A. Ambrosini, E. N. Coker, J. E. Miller, W. C. Chueh, R. O'Hayre and J. Tong, *Energy Procedia*, 2014, **49**, 2009–2018.
7 S. M. Babiniec, E. N. Coker, A. Ambrosini and J. E. Miller, *SolarPACES*, 2015, p. 050006.
8 J. N. Kuhn and U. S. Ozkan, *Catal. Lett.*, 2008, **121**, 179–188.
9 J. R. Scheffe, J. Li and A. W. Weimer, *Int. J. Hydrogen Energy*, 2010, **35**, 3333–3340.
10 C. L. Muhich, B. W. Evanko, K. C. Weston, P. Lichty, X. Liang, J. Martinek, C. B. Musgrave and A. W. Weimer, *Science*, 2013, **341**, 540–542.
11 T. Block and M. Schmücker, *Sol. Energy*, 2016, **126**, 195–207.
12 S. Abanades and G. Flamant, *Sol. Energy*, 2006, **80**, 1611–1623.
13 W. C. Chueh, C. Falter, M. Abbott, D. Scipio, P. Furler, S. M. Haile and A. Steinfeld, *Science*, 2010, **330**, 1797–1801.

14 Q.-L. Meng, C.-I. Lee, T. Ishihara, H. Kaneko and Y. Tamaura, *Int. J. Hydrogen Energy*, 2011, **36**, 13435–13441.
15 J. Scheffe, R. Jacot, G. R. Patzke and A. Steinfeld, *J. Phys. Chem. C*, 2013, **177**, 24104–24114.
16 W. C. Chueh and S. M. Haile, *ChemSusChem*, 2009, **2**, 735–739.
17 F. Call, M. Roeb, M. Schmücker, C. Sattler and R. Pitz-Paal, *J. Phys. Chem. C*, 2015, **119**, 6929–6938.
18 H. Kaneko, S. Taku and Y. Tamaura, *Sol. Energy*, 2011, **85**, 2321–2330.
19 C. Muhich and A. Steinfeld, *J. Mater. Chem. A*, 2017, **5**, 15578–15590.
20 D. A. Andersson, S. I. Simak, N. V. Skorodumova, I. A. Abrikosov and B. Johansson, *Proc. Natl. Acad. Sci. U. S. A.*, 2006, **103**, 3518–3521.
21 M. Mogensen, N. M. Sammes and G. A. Tompset, *Solid State Ionics*, 2000, **129**, 63–94.
22 W. C. Chueh and S. M. Haile, *Philos. Trans. R. Soc., A*, 2010, **368**, 3269–3294.
23 A. Morikawa, T. Suzuki, T. Kanazawa, K. Kikuta, A. Suda and H. Shinjo, *Appl. Catal., B*, 2008, **78**, 210–221.
24 A. Le Gal and S. Abanades, *J. Phys. Chem. C*, 2012, **116**, 13516–13523.
25 B. M. Reddy and A. Khan, *Catal. Surv. Asia*, 2005, **9**, 155–171.
26 D. A. Andersson, S. I. Simak, N. V. Skorodumova, I. A. Abrikosov and B. Johansson, *Phys. Rev. B: Condens. Matter Mater. Phys.*, 2007, **76**, 174119.
27 D. Marxer, P. Furler, J. Scheffe, H. Geerlings, C. Falter, V. Batteiger, A. Sizmann and A. Steinfeld, *Energy Fuels*, 2015, **29**, 3241–3250.
28 R. J. Panlener, R. N. Blumenthal and J. E. Garnier, *J. Phys. Chem. Solids*, 1975, **36**, 1213–1222.
29 B. Ravel and M. Newville, *J. Synchrotron Radiat.*, 2005, **12**, 537–541.
30 J. J. Mortensen, L. B. Hansen and K. W. Jacobsen, *Phys. Rev. B: Condens. Matter Mater. Phys.*, 2005, **71**, 035109.
31 J. Enkovaara, C. Rostgaard, J. J. Mortensen, J. Chen, M. Dułak, L. Ferrighi, J. Gavnholt, C. Glinsvad, V. Haikola, H. A. Hansen, H. H. Kristoffersen, M. Kuisma, A. H. Larsen, L. Lehtovaara, M. Ljungberg, O. Lopez-Acevedo, P. G. Moses, J. Ojanen, T. Olsen, V. Petzold, N. A. Romero, J. Stausholm-Møller, M. Strange, G. A. Tritsaris, M. Vanin, M. Walter, B. Hammer, H. Häkkinen, G. K. H. Madsen, R. M. Nieminen, J. Nørskov, M. Puska, T. T. Rantala, J. Schiøtz, K. S. Thygesen and K. W. Jacobsen, *J. Phys.: Condens. Matter*, 2010, **22**, 253202.
32 S. Bahn and L. W. Jacobsen, *Comput. Sci. Eng.*, 2002, **4**, 56–66.
33 Both ASE and GPAW are open-source code available from the Department of Physics at the Technical University of Denmark and are https://wiki.fysik.dtu.dk/ase/ and https://wiki.fysik.dtu.dk/gpaw/.
34 B. Hammer, L. B. Hansen and J. K. Nørskov, *Phys. Rev. B: Condens. Matter Mater. Phys.*, 1999, **59**, 7413–7421.
35 R. Michalsky, V. Botu, C. M. Hargus, A. A. Peterson and A. Steinfeld, *Adv. Energy Mater.*, 2015, **5**, 1401082.
36 V. Botu, R. Ramprasad and A. B. Mhadeshwar, *Surf. Sci.*, 2014, **619**, 49–58.
37 M. D. Krcha, A. D. Mayernick and M. J. Janik, *J. Catal.*, 2012, **293**, 103–115.
38 D. J. M. Bevan and J. Kordis, *J. Inorg. Nucl. Chem.*, 1964, **26**, 1509–1523.
39 Z. Zhao, M. Uddi, N. Tsvetkov, B. Yildiz and A. Ghoniem, *J. Phys. Chem. C*, 2016, **120**, 16271–16289.
40 R. D. Shannon and C. T. Prewitt, *Acta Crystallogr., Sect. B: Struct. Crystallogr. Cryst. Chem.*, 1969, **25**, 925–946.
41 Y. A. Daza and J. N. Kuhn, *RSC Adv.*, 2016, **6**, 49675–49691.
42 W. Huang, J. N. Kuhn, C.-K. Tsung, Y. Zhang, S. E. Habas, P. Yang and G. A. Somorjai, *Nano Lett.*, 2008, **8**, 2027–2034.
43 T. Bunluesin, R. J. Gorte and G. W. Graham, *Appl. Catal., B*, 1998, **15**, 107–114.
44 B. Harrison, A. F. Diwell and C. Hallett, *Platinum Met. Rev.*, 1988, **32**, 73–83.
45 G. Rao and H. Sahu, *Proc. - Indian Acad. Sci., Chem. Sci.*, 2001, **113**, 651–658.
46 M. E. Galvez, R. Jacot, J. Scheffe, T. Cooper, G. R. Patzke and A. Steinfeld, *Phys. Chem. Chem. Phys.*, 2015, **17**, 6629–6634.
47 M. Guo, J. Lu, Y. Wu, Y. Wang and M. Luo, *Langmuir*, 2011, **27**, 3872–3877.
48 B. M. Reddy, G. K. Reddy, L. H. Reddy and I. Ganesh, *Open Phys. Chem. J.*, 2009, **3**, 24–29.
49 X. M. Lin, L. P. Li, G. S. Li and W. H. Su, *Mater. Chem. Phys.*, 2001, **69**, 236–240.
50 H. Liang, J. M. Raitano, G. He, A. J. Akey, I. P. Herman, L. Zhang and S.-W. Chan, *J. Mater. Sci.*, 2012, **47**, 299–307.
51 R. C. Karnatak, *J. Alloys Compd.*, 1993, **192**, 62–68.
52 P. Singh, M. S. Hegde and J. Gopalakrishnan, *Chem. Mater.*, 2008, **20**, 7268–7273.
53 J. Wong, F. W. Lytle, R. P. Messmer and D. H. Maylotte, *Phys. Rev. B: Condens. Matter Mater. Phys.*, 1984, **30**, 5596–5610.
54 W. C. Chueh, A. H. McDaniel, M. E. Grass, Y. Hao, N. Jabeen, Z. Liu, S. M. Haile, K. F. McCarty, H. Bluhm and F. El Gabaly, *Chem. Mater.*, 2012, **24**, 1876–1882.
55 M. Burbano, S. Nadin, D. Marrocchelli, M. Salanne and G. W. Watson, *Phys. Chem. Chem. Phys.*, 2014, **16**, 8320–8331.
56 E. Tani, M. Yoshimura and S. Somiya, *J. Am. Ceram. Soc.*, 1983, **66**, 506–510.
57 G. Henkelman, A. Arnaldsson and H. Jónsson, *Comput. Mater. Sci.*, 2006, **36**, 354–360.
58 M. Takacs, J. R. Scheffe and A. Steinfeld, *Phys. Chem. Chem. Phys.*, 2015, **17**, 7813–7822.
59 Y. Hao, C.-K. Yanga and S. M. Haile, *Phys. Chem. Chem. Phys.*, 2013, **15**, 17084–17092.
60 D. Marxer, P. Furler, M. Takacs and A. Steinfeld, *Energy Environ. Sci.*, 2017, **10**, 1142–1149.
61 M. Ezbiri, M. Takacs, B. Stolz, J. Lungthok, A. Steinfeld and R. Michalsky, *J. Mater. Chem. A*, 2017, **5**, 15105–15115.
62 P. P. Sahoo, J. L. Payne, M. Li, J. B. Claridge and M. J. Rosseinsky, *J. Phys. Chem. Solids*, 2015, **76**, 82–87.